



Bifunctional Pt dual atoms for overall water splitting

Pengfei Zhang^{a,1}, Manyuan Gan^{a,1}, Yanhui Song^{a,b,c,*}, Peizhi Liu^a, Haojie Liang^a,
Yongqing Shen^a, Bingshe Xu^d, Ting Liao^{e,f}, Junjie Guo^{a,c,*}, Ziqi Sun^{b,f,**}

^a Key Laboratory of Interface Science and Engineering in Advanced Materials, Ministry of Education, Taiyuan University of Technology, Taiyuan 030024, P.R. China

^b School of Chemistry and Physics, Queensland University of Technology, Brisbane, QLD 4001, Australia

^c Instrumental Analysis Center Taiyuan University of Technology, Taiyuan 030024, P.R. China

^d Materials Institute of Atomic and Molecular Science, Shaanxi University of Science and Technology, Xi'an 710021, P.R. China

^e School of School of Mechanical, Medical and Process Engineering, Queensland University of Technology, Brisbane, QLD 4001, Australia

^f Centre for Materials Science, Queensland University of Technology, Brisbane, QLD 4001, Australia

ARTICLE INFO

Keywords:

Pt dual-atom catalyst
Interatomic distance
Overall water splitting

ABSTRACT

While dual-atom catalysts benefiting from synergetic interatomic interactions have inspired the development of emerging catalysts, the role of atomic interactions on the catalytic selectivity and activity has yet to be clearly discovered. Herein, two-types of Pt dual-atom active sites, Pt dimers (2Pt) with an interatomic distance of 2.6 Å and Pt pairs (Pt₂) at a distance of 0.9 Å, are fabricated by anchoring onto cationic vacancy-rich nickel-based hydroxide (Pt@NiFeCo-E). It reveals that 2Pt sites are favorable for hydrogen evolution reaction (HER) while Pt₂ sites are active towards oxygen evolution reaction (OER). The coexistence of two types of Pt dual atoms endows the bifunctional activity, which reached an overpotential of 14 mV@10 mA cm⁻² for HER, an overpotential of 234 mV@100 mA cm⁻² for OER, and an effective overall water splitting reaction (OWS) in alkaline at an overpotential of 1.42 V to reach 10 mA cm⁻² and at 100 mA cm⁻² for 50 h. This work not only clarifies a new mechanism in manipulating the selectivity of dual-atom catalysts via controlling the interatomic distance, but also paves a pathway for designing novel high-efficient bifunctional catalysts.

1. Introduction

Green hydrogen energy generated from water splitting has been considered as an ideal alternative energy, due to its high energy density and zero emission [1–3]. As the reverse reaction of a spontaneous water formation reaction from hydrogen and oxygen, very high energy barrier and sluggish kinetic process exist in the two-half reactions of water splitting, i.e., hydrogen evolution reaction (HER) and oxygen evolution reaction (OER), which request undesired high energy input [4,5]. Even though the employment of commercial Pt/C and Ir/Ru oxide catalysts could significantly lower the energy consumption, the earth scarcity and high-cost has hampered the production of affordable hydrogen [6–9]. In this respect, an effective strategy is maximizing the atom utilization and catalytic activity by forming atomically dispersed single-atom catalysts (SACs) [10]. For instance, Yu et al. synthesized Pt single-atom catalyst by anchoring oxygen vacancies in NiCo LDHs with Pt, resulting in an

excellent electrocatalytic performances for HER//GOR with a cell voltage of only 1.37 V at 100 mA cm⁻² [11], Kuang et al. developed Pt single-atom supported on N-doped mesoporous hollow carbon spheres via strong electronic metal–support interaction engineering, which greatly enhanced HER electrocatalytic activity (40 mV@10 mA cm⁻²) [12].

Very recently, dual-atom catalysts (DACs) have been explored as another emerging SACs [13–16], which present interesting synergetic catalytic activity from the neighboring atomic interactions in addition to the merits of single atoms [17,18]. For example, a series of Co-M (M = Fe, Cu, Zn) dual atoms supported on carbon paper have been fabricated for HER catalysis (90 mV @ 20 mA cm⁻²) [19], and Co-Co dual atoms loaded on N-doping hollow carbon spheres demonstrated excellent HER, OER, and oxygen reduction reaction (ORR) activities. Despite the boosted catalytic activity contributed by the synergetic dual-atom interactions, the roles of interatomic distance and local coordination

* Corresponding authors at: Key Laboratory of Interface Science and Engineering in Advanced Materials, Ministry of Education, Taiyuan University of Technology, Taiyuan 030024, P.R. China.

** Corresponding author at: School of Chemistry and Physics, Queensland University of Technology, Brisbane, QLD 4001, Australia.

E-mail addresses: songyanhui@tyut.edu.cn (Y. Song), guojunjie@tyut.edu.cn (J. Guo), ziqi.sun@qut.edu.au (Z. Sun).

¹ P. Zhang and M. Gan are contributed equally to this work.

environments in the activity enhancement of dual-atom catalysts are yet not clearly investigated [20].

In this work, a bifunctional Pt dual-atom catalyst constituting of two types of Pt dual atoms, Pt dimers (2Pt) with an interatomic distance of 2.6 Å and Pt pairs (Pt₂) with a distance of 0.9 Å anchoring on cationic vacancy-rich nickel-based layered double hydroxide (Pt@NiFeCo-E) substrate were fabricated. It reveals that the interatomic distances of the Pt dual atoms are closely related with their catalytic activity. The 2Pt is favorable for HER catalysis and the Pt₂ structure is more active to OER catalysis, by which a bifunctionality of Pt towards overall water splitting (OWS) catalysis is reached. The electrochemical cell with Pt@NiFeCo-E//Pt@NiFeCo-E electrodes only needs 1.42 V to reach 10 mA cm⁻² for OWS and exhibits robust stability to operate at 100 mA cm⁻² for more than 50 h, showing its promising potential in practical applications. Furthermore, this catalyst is also very highly efficient and stable for overall splitting of real seawater. This work, therefore, provides a new strategy for designing bifunctional noble-metal-based catalysts at a minimized active metal load.

2. Experimental

2.1. Catalyst preparation

NiFeCo was synthesized via a typical hydrothermal method. First, 1 mmol Co(NO₃)₂·6H₂O, 1 mmol Fe(NO₃)₃·9H₂O, 5 mmol urea and 4 mmol NH₄F were dissolved in 36 mL of ultrapure water and stirred until completely dissolved. Then, adding NF (4 cm × 2 cm) into the solution, and transferred to 50 mL stainless-steel Teflon-lined autoclave. Ultimately, the autoclave was airtight heated at 180 °C lasting for 10 h followed by cooling down to room temperature naturally. Then wash with a lot of water and ethanol respectively, and dry at 60 °C overnight.

The preparation of NiFeCo-E is based on the preparation of NiFeCo and then through the following treatment. First, the NiFeCo (1 cm × 2 cm) was immersed in a 10 mL NaOH solution (5 M), and then the solution was heated to 90 °C in an oil bath for 10 min and kept for 90 min. Subsequently, the samples were washed and dried with water and ethanol. The etching time (x, min) was changed as the control group, and the catalyst was named NiFeCo-E(x), where x = 0/30/60/120. It is worth noting that when x = 0, the name of the catalyst is NiFeCo. When x = 90, the name of the catalyst is NiFeCo-E.

NiFeCo-E (2 cm × 2 cm) was dispersed into 10 mL of H₂PtCl₆ (1 g L⁻¹) water solution. Kept it at room temperature for 160 min. Then washed with a lot of water and ethanol respectively and dried at 60 °C overnight to obtain Pt@NiFeCo-E. The etching time (x, min) and immersion time (y, min) were changed as the control group, and the catalyst was named (y)Pt@NiFeCo-E(x), where x = 0/30/60/90/120, y = 0/40/80/120/160/200. It is worth noting that when x = 90, y = 0, the name of the catalyst is NiFeCo-E. When x = 0, y = 160, the name of the catalyst is Pt@NiFeCo. For comparison, the unetched sample Pt@NiFeCo was prepared by the similar method.

2.2. Materials characterization

Morphology and structure of the materials were characterized using a FIB-SEM crossbeam workstation (TESCAN, LYRA 3 XMH) operating at an accelerating voltage of 20 kV and a transmission electron microscopy (TEM, JEOL, JEM-F200) working at an acceleration voltage of 200 kV. The energy dispersive spectroscopy (EDS) was collected using EDS system equipped on TEM. Scanning transmission electron microscopy (STEM) in the high angle annular dark field mode (HAADF-STEM) were acquired by using a JEOL ARM 300F² operating at 300 kV. Additionally, the powder X-ray diffraction (XRD) pattern was analyzed through Japanese science Ultima IV with a Cu Kα X-ray source (λ = 1.54178 Å) to elaborate phase expansion and crystal structure of the samples. X-ray photoelectron spectroscopy (XPS) measurements were performed to determine the chemical bonding states using an Amicus from 10 kV Mg

Kα radiation at the pressure of 1 × 10⁻⁷ Par. The Raman spectra was used to analyze the vibrational rotational energy levels of substances through Renishaw inVia Microscopic confocal Raman spectroscopy equipped with a 532 nm laser excitation source. Chemical compositions of the synthesized samples were examined by ICP-OES (720 ICP-OES, Agilent Technologies). X-ray absorption fine structure (XAFS) spectra were collected using an Easy XES150 system (Easy XAFS LLC, USA), and the data were analyzed by the Athena software.

3. Results and discussion

To facilitate the dispersion of Pt single atoms, a cationic vacancy-rich NiFeCo layered double hydroxide (NiFeCo-E) was employed as the substrate to form a Pt dual-atom catalyst (Pt@NiFeCo-E), where two types of Pt dual-atomic structures, as shown in Fig. 1a, Pt dimers with an interatomic distance of 2.6 Å (2Pt) and Pt pairs with a distance of 0.9 Å (Pt₂), were anchored onto the support substrates. As described in the Supporting Information, FeCo layered double hydroxide nanosheets on Ni-foam (FeCo-LDH@Ni) were first synthesized by a facile hydrothermal method and then treated by ammonium fluoride (NH₄F) in an autoclave at 180 °C for 10 h to get Ni-based LDH (NiFeCo-LDH, Ni:Fe:Co = 5:1:1 according to the ICP-OES characterization, Table S1). Then, further etching the NiFeCo-LDH in 5 M NaOH, a Ni-based vacancy-rich NiFeCo-LDH support was obtained (NiFeCo-E, Ni:Fe:Co = 4.6:1:1). Pt deposition was carried out by immersing the NiFeCo-E into the aqueous H₂PtCl₆ solution and soaking for 0–200 min, followed with alternative water and ethanol washing, and drying at 60 °C overnight.

Fig. 1b presents the nanosheet morphology of Pt@NiFeCo-E on the NF substrate, which is similar to the morphologies of the Ni-based LDHs with or without treatment (Fig. S1). Both the high resolution transmission electron microscope (HRTEM) (Fig. 1c and S2) and XRD characterizations (Fig. 1d) reveal that the NiFeCo-E is composed of NiFe(Co)-LDH and Ni(Co)(OH)₂. As identified from the lattice fringes, the lattice spacing of 0.26 nm could be assigned to the (012) lattice planes of NiFe-LDH and the lattice with a space of 0.15 nm could be the (111) plane of Ni(OH)₂. The XRD patterns (Fig. 1d) reveal that the Ni-based LDHs before and after treatment were composed of Ni-Fe(Co) LDH (PDF#40–0215) and Ni(OH)₂ (PDF#14–0117), which is consistent with the TEM results. Observing the diffraction peaks at 11.4° (Fig. S3), corresponding to the (003) plane of Ni-Fe(Co) LDH, slight shifting of the peak to the left happened after Pt anchoring, which should be the lattice expansion resulted by Pt anchoring at the vacancy sites [21]. The chemical compositions (Table S1) and the EDS mapping of Pt@NiFeCo-E (Fig. 1e) all demonstrated the homogeneously dispersion of Co, Fe, Ni, O, and Pt elements. Especially, the Co-content was even higher than that of Fe, which could be resulted by the partial substitution of Fe³⁺ (69 pm) by Co³⁺ (68.5 pm) with similar ion radii. Therefore, the NiFe-LDH phase identified by both XRD and TEM should be actually NiFeCo-LDH phase.

HAADF-STEM (Fig. 1f and S4) analyses on different regions confirmed the 2Pt dimer and Pt₂ pair structure evenly dispersed in Pt@NiFeCo-E catalyst. As marked in Fig. 1g, among the 253 couples of 2Pt dimers and Pt₂ pairs countered on the views, 184 were 2Pt dimers and 67 were Pt₂ pairs, of which 2Pt dimers are around 73.3 %. It has been reported that the distance of 2.6 Å in 2Pt dimers enables the well adsorption of two H atoms of H₂O molecules on them, thereby stretching the bond of H₂O to activate the formation of H* intermediates during HER process [22]. In contrast to the homogeneous distribution of 2Pt and Pt₂ dual-atoms, the deposition of Pt on non-vacancy NiFeCo-LDH substrate (Pt@NiFeCo) are mostly in the form of small clusters of multiple atoms, revealing the critical role of vacancy in anchoring Pt dual atomic structures (Fig. S5). The mass loading of the Pt species (Table S1) in Pt@NiFeCo-E was determined to be 9.04 wt. % by an ICP-OES method, revealing the adsorption affinity of NiFeCo-E substrate towards Pt atoms. According to XPS and EDS results (Table S2), NiFeCo-E had a higher O content, corresponding to higher cation vacancies, which play critical role in anchoring and forming Pt dual-atoms [23].

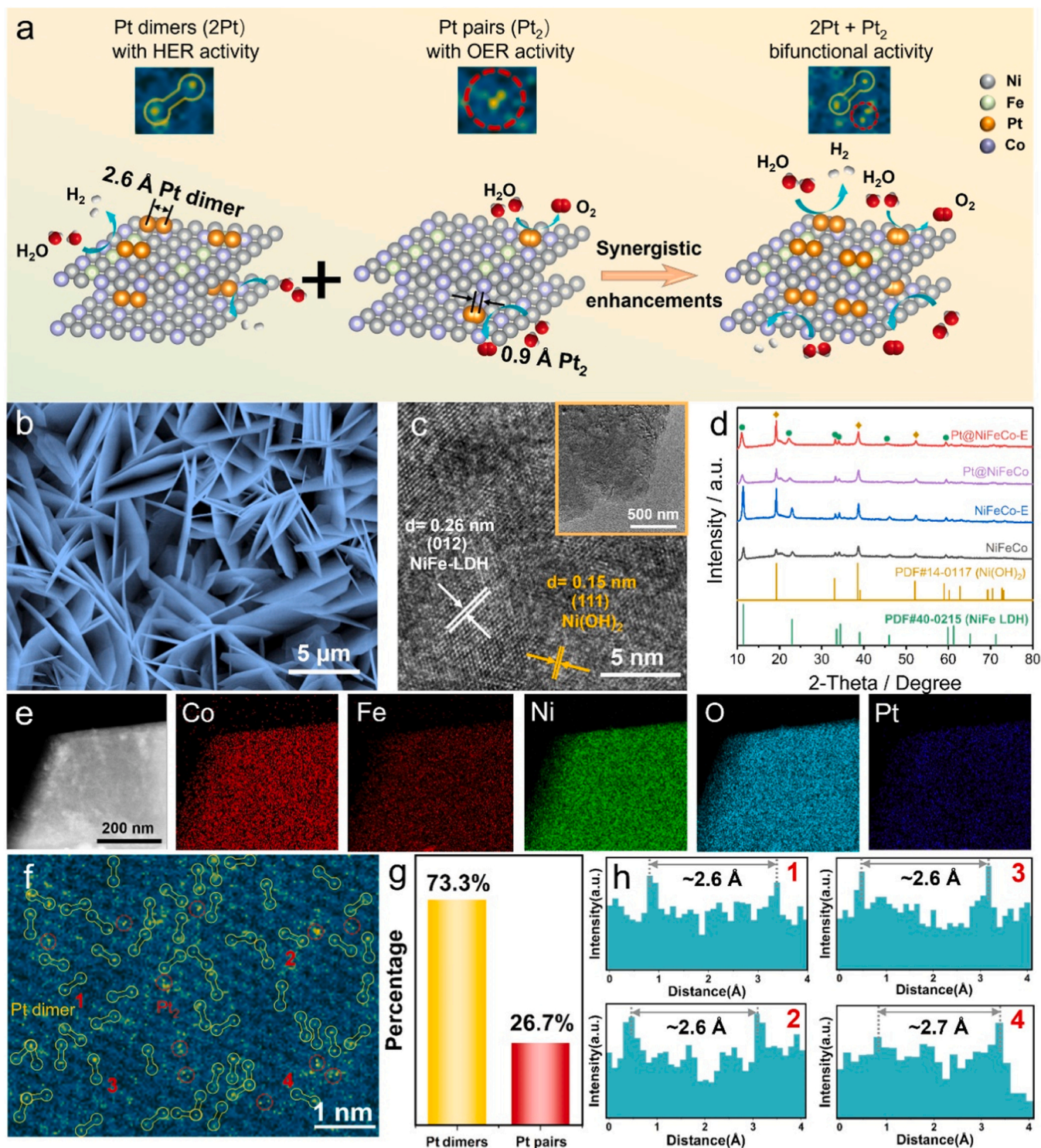


Fig. 1. Pt dimers (2Pt) and Pt pairs (Pt₂) synthesized on cationic vacancy NiFeCo LDH (NiFeCo-E) substrate. (a) Schematic illustration of Pt dimers and Pt pairs on NiFeCo-E and their bifunctionality towards water splitting catalysis. (b) SEM image of Pt loaded etched NiFeCo LDH (Pt@NiFeCo-E). (c) TEM image of Pt@NiFeCo-E, the inset is the low magnification TEM image. (d) XRD patterns of NiFeCo LDH, NiFeCo-E, Pt loaded NiFeCo LDH (Pt@NiFeCo), and Pt@NiFeCo-E. (e) TEM-EDS elemental mapping images of Pt@NiFeCo-E. (f) Atomic-resolution HAADF-STEM image of Pt@NiFeCo-E. (g) A statistical diagram of Pt dimers and Pt₂. (h) Intensity profiles showing the interatomic distance of two types of Pt dual atoms.

Fig. 2a presents the Raman spectra collected on both the unloaded and Pt loaded NiFeCo and NiFeCo-E. In NiFeCo-E substrate, two representative peaks located at 459 and 520 cm⁻¹ could be assigned to the E_{g1} bending vibration and the A_{1g} stretching vibration modes of nickel oxides (Ni²⁺-OH and Ni²⁺-O) vibrations [24–26]. One other less-obvious band located at 323 cm⁻¹ is the characteristic peaks of hydroxyl (O-H)

groups, and the one at 1044 cm⁻¹ should be from the adsorbed carbonate/nitrate anions. After Pt loading, the peak positions of Ni-O(H) species in Pt@NiFeCo and Pt@NiFeCo-E were slightly shifted to higher wavenumbers, indicating the Pt anchoring induced lattice expansion [27]. It is worth noting that a distinct peak at 596 cm⁻¹ appeared in the etched samples, which corresponds to the hydroxyl

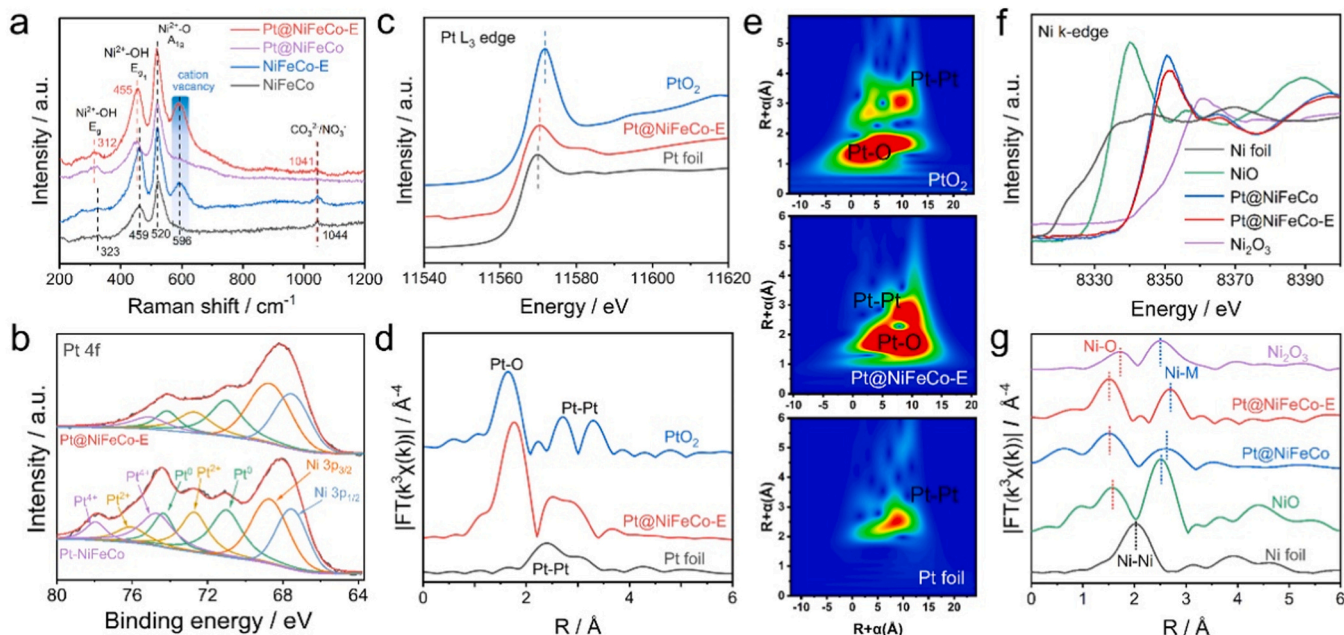


Fig. 2. Electronic structure characterizations of Pt@NiFeCo-E. (a) Raman spectra of NiFeCo, NiFeCo-E, Pt@NiFeCo, and Pt@NiFeCo-E. (b) XPS spectra of Pt 4f peaks for Pt@NiFeCo and Pt@NiFeCo-E. (c) Pt L₃-edge XANES and (d) EXAFS of Pt@NiFeCo-E, Pt foil, and PtO₂. (e) WT contour plots of Pt L₃-edge at R space of Pt@NiFeCo-E, Pt foil, and PtO₂. (f) Ni k-edge XANES spectra and (g) EXAFS of Pt@NiFeCo, Pt@NiFeCo-E, Ni foil, NiO, and Ni₂O₃.

group vibration near the defect sites [28,29], confirming the formation of cation vacancies. The appearance of strong vacancy induced vibration and the formation of homogeneous Pt dual-atoms in Pt@NiFeCo-E indicate that the formation of cationic vacancies are the critical sites to anchoring Pt dual atoms without agglomerating into clusters.

The elemental chemical states analyses were carried out via XPS characterizations. Fig. 2b and S6–7 displayed the XPS spectra of Pt 4f, Ni 2p, Co 2p, Fe 2p, and O 1s of the prepared samples. The Ni 2p (Fig. S6a) and Co 2p (Fig. S6b) indicate the coexistence of Ni²⁺ (855.72 eV Ni 2p_{3/2} and 873.36 eV Ni 2p_{1/2}) and Ni³⁺ (856.90 eV Ni 2p_{3/2} and 874.91 eV Ni 2p_{1/2}) together with the appearance of Co²⁺ and Co³⁺ species, indicating the substitution of Co to Ni in the NiFe-LDH structure. Moreover, there are the existence of their satellite peaks at 786.90 and 802.91 eV [30]. In the Fe 2p spectra (Fig. S6c), negative shifting of 0.35 eV on the binding energy of Fe³⁺ in Pt@NiFeCo-E and Pt@NiFeCo compared with the unloaded samples was observed, demonstrating increased electron density transfer from the loaded Pt atoms to Fe [31]. For Pt@NiFeCo-E, the peaks located at the binding energies of 71.00 and 74.35 eV assign to Pt 4f_{7/2} and Pt 4f_{5/2} of Pt⁰ species (Fig. 2b), and we attribute two peaks of 72.70 and 76.05 eV to Pt 4f_{7/2} and Pt 4f_{5/2} of Pt²⁺ species. Meanwhile, the Pt⁴⁺ species are also affirmed by another two peaks at 74.70 and 77.95 eV for Pt 4f_{7/2} and Pt 4f_{5/2} [32]. For Pt 4f core levels, the species of Pt⁰, Pt²⁺, and Pt⁴⁺ were identified in both Pt@NiFeCo and Pt@NiFeCo-E, but shifts to a positive direction in the etched sample as the formation of cation vacancies have been observed [33]. Similarly, strong electronic interactions and electron transfers also confirmed in the O 1s spectra collected on Pt@NiFeCo-E (Fig. S6d), providing additional evidence on the formation of cationic vacancies and the anchoring of Pt dual atoms.

X-ray absorption near-edge structure (XANES) and extended X-ray absorption fine structure measurements (EXAFS) were conducted to further investigate the chemical states and coordination environments of Pt, Ni, Fe, and Co atoms in the catalysts. As shown in the Pt L₃-edge XANES spectra (Fig. 2c), the white line position of Pt@NiFeCo-E situates between those of the Pt foil and the PtO₂, indicating that the oxidation state of the Pt atoms in Pt@NiFeCo-E is between 0 and +4, which agrees well with the XPS analyses. The EXAFS results further provide information on the coordination environment of the Pt atoms. As shown in

Fig. 2d, Pt in Pt@NiFeCo-E has two prominent peaks, which are attributed to the Pt-O and the Pt-M (Fe, Co, Ni and Pt) at 1.77 Å and 2.52 Å, respectively. The bond distance of Pt-M is slightly longer than that of the metallic Pt-Pt but shorter than that of the PtO₂, which accounts for the single-atom feature, ruling out the presence of Pt clusters or nanoparticles [34]. The phase difference between the Pt-O formed in Pt@NiFeCo-E and the PtO₂ suggests the different O coordination numbers surrounding Pt [35,36]. In addition, the wavelet transforms contour plots of Pt in Pt@NiFeCo-E revealed two intensities maximum of around 1.8 Å⁻¹ and 2.5 Å⁻¹ (Fig. 2e), which corresponds to Pt-O and Pt-M coordinations in Pt@NiFeCo-E. Fig. 2f and S8a–b display the Ni, Fe, and Co k-edge XANES spectra. The oxidation states of Ni are located between +2 and +3 (Fig. 2g). While the valance state of Fe in Pt@NiFeCo-E and Pt@NiFeCo is closer to +3 (Fig. S8c), the valance state of Co is at the middle of +2 and +3. We also noted the absorption threshold position of Ni, Fe, and Co in Pt@NiFeCo-E shifted to higher energies compared to those of Pt@NiFeCo, confirming that the slightly increased oxidation state in Pt@NiFeCo-E (Fig. 2f and S8a–b), which are associated with the formation of cationic vacancies after etching. Fig. 2g and S8c–d reveals the existence of both metal-O and metal-metal coordination in the synthesized samples [37]. The increased intensity of pre-edge peaks at about 7103.6 eV for Fe and 8335.0 eV for Ni in the k-edge XANES spectra (Fig. S9) indicate the lower coordination and asymmetric configurations of the metal centers, further confirmed the existence of defects around the metal sites [38].

The electrochemical catalytic performance towards water splitting reactions were evaluated via a standard procedure as described in Supporting Information. The reference electrode is calibrated prior to testing (Fig. S10). First, to optimize the etching time and Pt loading time on the performance of Pt@NiFeCo-E catalysts, both the HER and OER activities of the Pt@NiFeCo-E catalysts prepared with different etching time in NaOH and soaking time in chloroplatinic acid were examined. As shown in Figs. S11–12, the Pt@NiFeCo-E etched for 90 min and soaked for 160 min showed the best electrocatalytic performance, which was then selected as the optimized Pt@NiFeCo-E catalyst for following comparison studies. The HER catalytic performances of nickel foam (NF), untreated NiFeCo-LDH (NiFeCo), etched NiFeCo-LDH (NiFeCo-E), Pt loaded on unetched NiFeCo-LDH (Pt@NiFeCo), and optimized Pt

loaded on etched NiFeCo-LDH (Pt@NiFeCo-E) were evaluated in a standard three-electrode cell with 1.0 M KOH aqueous electrolyte. As illustrated in Fig. 3a, Pt@NiFeCo-E only required an overpotential of 14 mV to reach a current density of 10 mA cm^{-2} , which are much lower than that of NF (228 mV), NiFeCo (219 mV), NiFeCo-E (172 mV), Pt@NiFeCo (27 mV), Pt/C (18 mV). This super low overpotential of Pt@NiFeCo-E in the alkaline electrolyte outperforms most of previously reported Pt-based HER catalysts (Table S3 and Fig. 3h). To further evaluate the catalytic activity, the mass activity (MA) and turnover frequency (TOF) were calculated. As shown in Fig. S13, The MA of Pt@NiFeCo-E (0.71 A mg^{-1}) at 70 mV was nearly 24 times greater than that of Pt/C (0.03 A mg^{-1}). Additionally, the TOF for Pt@NiFeCo-E electrode (0.72 s^{-1}) showed 24 and 1.9 times higher than that of the Pt/C catalyst (0.03 s^{-1}) and the Pt@NiFeCo (0.38 s^{-1}), respectively. The Tafel slope of Pt@NiFeCo-E was only $22.37 \text{ mV dec}^{-1}$, which is also smaller than the control samples of NF ($151.15 \text{ mV dec}^{-1}$), NiFeCo ($126.15 \text{ mV dec}^{-1}$), NiFeCo-E ($68.62 \text{ mV dec}^{-1}$) and Pt@NiFeCo ($64.76 \text{ mV dec}^{-1}$) (Fig. S14a). The lower Tafel slope means the better HER kinetics and the more promising potential for high current catalysis [31,39]. The Tafel slope of $22.37 \text{ mV dec}^{-1}$ for Pt@NiFeCo-E indicates the rate determining step is the Tafel step, and the slope of 64.76 mV

dec^{-1} for Pt@NiFeCo suggests the rate determining step is Heyrovsky step as most of Pt-based catalysts, while the rate determining step for NF and NiFeCo is the Volmer step [40,41]. The HER in alkaline conditions has much sluggish kinetics resulted by the supply of protons from an additional water dissociation step. It has been reported that the combination of metallic HER catalyst with an optimal H^* adsorption behavior with the water dissociation favorable oxides can provide low-energy barrier HER catalysis in an alkaline condition, which should be the origination of the fascinating HER catalytic activity of Pt@NiFeCo-E [42]. The electronic transfer kinetics of the catalysts were also examined by EIS. As shown in Fig. S15a, the Nyquist plot shows that the Pt@NiFeCo-E possessed the lowest charge transfer resistance (R_{ct} , 3.84Ω), validating the fastest HER electron transfer kinetics among the examined catalysts (as show in Table S4), the R_{ct} values of NF, NiFeCo, NiFeCo-E, and Pt@NiFeCo are 73.89, 68.67, 45.65, and 8.53Ω , respectively [43].

The OER performances were assessed in 1.0 M KOH. As displayed in Fig. 3d, the Pt@NiFeCo-E exhibited an excellent OER activity with a 234 mV overpotential to reach 100 mA cm^{-2} , which is superior to reference catalysts of NF (445 mV), NiFeCo (287 mV), NiFeCo-E (285 mV), and Pt@NiFeCo (247 mV). This OER overpotential is also

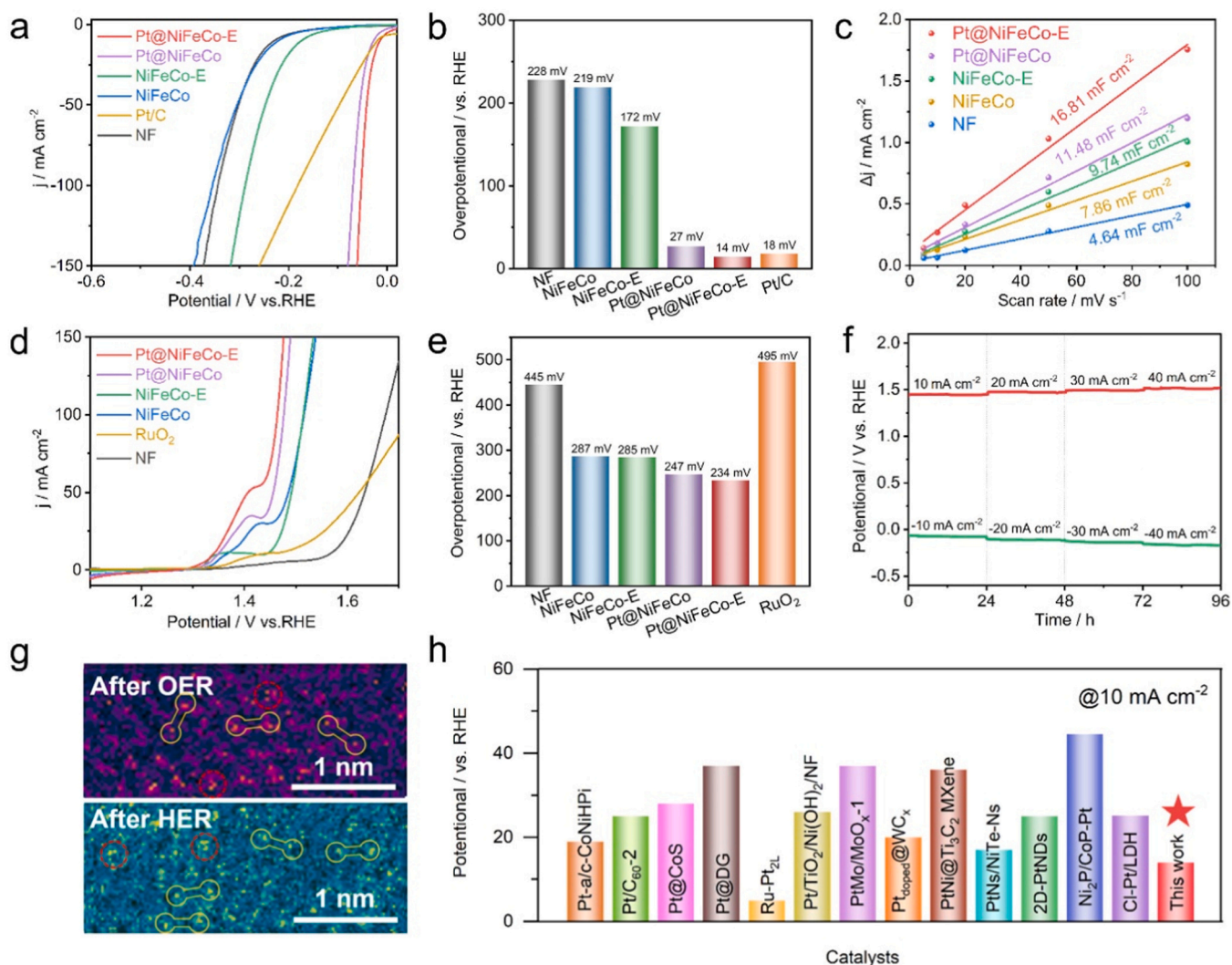


Fig. 3. HER and OER performance in 1.0 M KOH. (a) LSV curves for HER. (b) HER overpotentials of catalysts measured at a current density of 10 mA cm^{-2} . (c) Capacitive Δj versus scan rates at 1.14 V of selected catalysts. (d) LSV curves for OER. (e) OER overpotentials of catalysts measured at a current density of $10, 20, 30$, and 40 mA cm^{-2} for 96 h. (f) Chronopotentiometric tests of HER and OER for Pt@NiFeCo-E at a current density of $10, 20, 30$, and 40 mA cm^{-2} for 96 h. (g) HAADF-STEM of Pt@NiFeCo-E after chronopotentiometric tests. (h) Comparison of HER overpotentials @ 10 mA cm^{-2} in alkaline conditions of Pt@NiFeCo-E catalyst with other reported Pt-based catalysts.

lower than most of the recently reported works (Table S5). Fig. S14b presents the Tafel slopes, where the Pt@NiFeCo-E showed the lowest Tafel slope ($43.24 \text{ mV dec}^{-1}$) among the examined samples of NF ($93.69 \text{ mV dec}^{-1}$), NiFeCo ($83.37 \text{ mV dec}^{-1}$), NiFeCo-E ($51.29 \text{ mV dec}^{-1}$), and Pt@NiFeCo (45.4 mV dec^{-1}), indicating that Pt@NiFeCo-E has the fastest reaction kinetic [39,44]. Similar to HER, the Pt@NiFeCo-E possessed the lowest R_{ct} value (0.98Ω), compared with

114.2, 2.16, 1.69, and 1.46Ω , respectively, for NF, NiFeCo, NiFeCo-E, and Pt@NiFeCo, indicating the fastest OER electron transfer kinetics (Fig. S15b and Table S6). Furthermore, the electrochemical active surface areas of the catalysts were evaluated by measuring the C_{dl} values (Fig. 3c and S16). Again, the Pt@NiFeCo-E possessed the highest C_{dl} value (16.81 mF cm^{-2}) compared with others (4.64 mF cm^{-2} for NF, 7.86 mF cm^{-2} for NiFeCo, 9.74 mF cm^{-2} for NiFeCo-E and 11.48 mF cm^{-2}

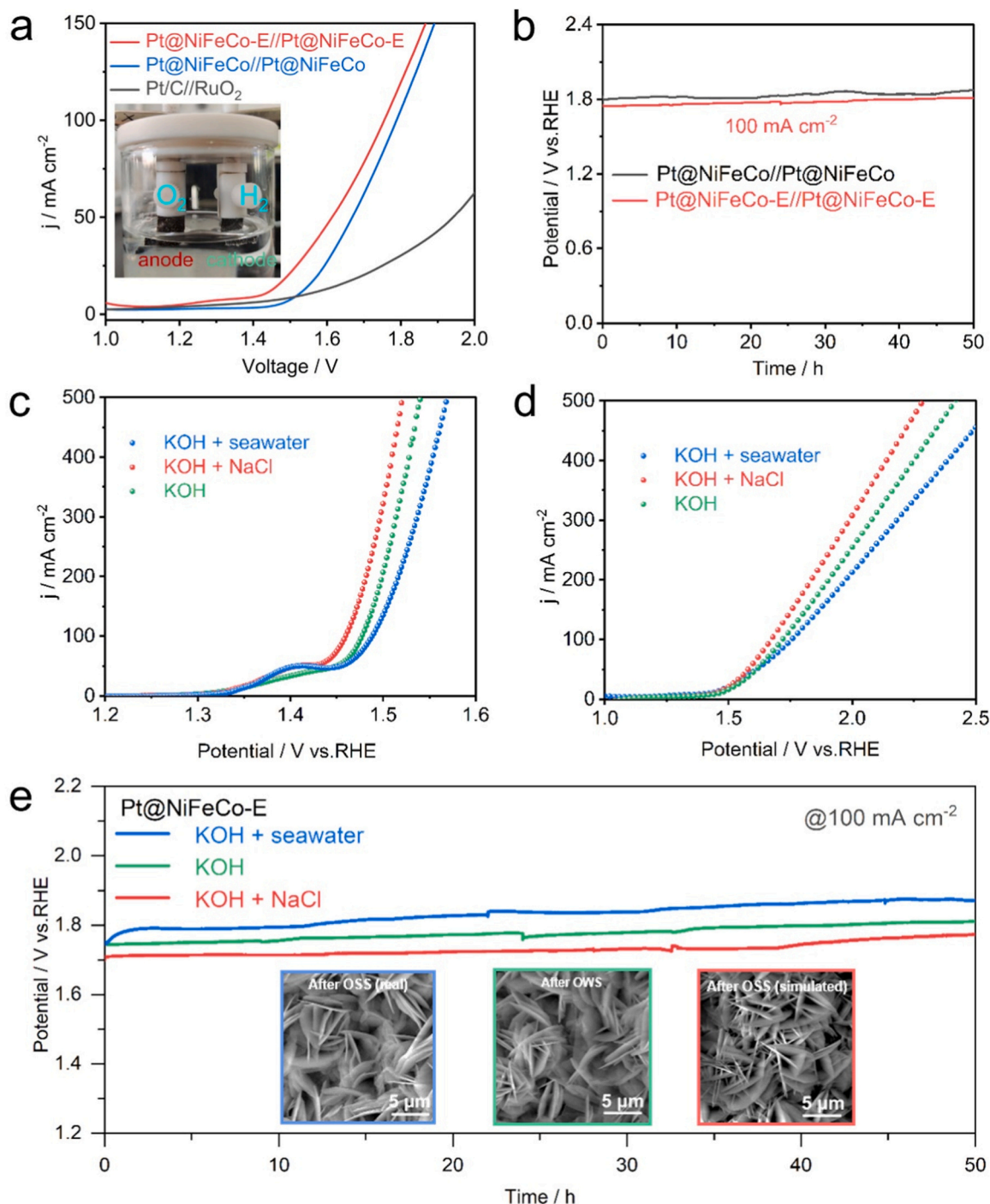


Fig. 4. Overall water splitting (OWS) catalysis performance for freshwater and real seawater. (a) OWS performance of the cells with Pt@NiFeCo-E//Pt@NiFeCo-E and Pt@NiFeCo//Pt@NiFeCo configurations in comparison with benchmark Pt/C//RuO₂ electrodes. The inset is optical image of a Pt@NiFeCo-E//Pt@NiFeCo-E cell with in 1.0 M KOH. (b) Chronopotentiometric curves of OWS for Pt@NiFeCo//Pt@NiFeCo and Pt@NiFeCo-E//Pt@NiFeCo-E cells at 100 mA cm^{-2} for 50 h. (c) The LSV curves for OER of Pt@NiFeCo-E in simulated seawater constituting of 1.0 M KOH, 1.0 M KOH, and 0.5 M NaCl and alkalized real seawater with 1.0 M KOH. (d) LSV curves for overall splitting of alkalized freshwater, simulated seawater, and real seawater by using Pt@NiFeCo-E as both anode and cathode. (e) Chronopotentiometric curves of overall splitting of alkalized freshwater, simulated seawater, and real seawater for Pt@NiFeCo-E//Pt@NiFeCo-E at 100 mA cm^{-2} for 50 h; the insets showing the morphologies after tests.

cm^{-2} for Pt@NiFeCo), indicating more catalytically active sites exposed on the surface [31].

Besides catalytic activity, the long-term stability of electrocatalysts is another critical indicator. The durability of Pt@NiFeCo-E for both HER and OER were measured via chronopotentiometric tests at current densities of 10, 20, 30, and 40 mA cm^{-2} . As shown in Fig. 3f, no obvious potential degradation was observed after 96 h of HER and OER stability tests, demonstrating a robust durability in alkaline for both the HER and OER catalysis. After the HER and OER stability tests, the morphology had no change (Fig. S17). It is more critical that, after the HER and OER stability tests, the Pt dimers and Pt₂ pairs were uniformly distributed on the carrier without the formation of multi-atom clusters and nanosized aggregations (Fig. 3g), which confirms excellent HER and OER stability of the Pt dual-atomic structures in the alkaline solutions. Furthermore, there were no variations in the phase of Pt@NiFeCo-E as well as the chemical state of all elements after the stability tests as demonstrated by the XRD and XPS characterizations. As shown in Fig. S18–19, the XRD diffraction peaks and XPS core levels of Pt, Co, Ni, and Fe of the post-testing catalysts did not present any shifting, except for the peaks of O 1s presented slight deviation as the result of electrochemical redox reactions. Based on the electrochemical catalysis characterizations, it is very clear that the Pt@NiFeCo-E catalyst has bifunctional catalytic activities towards both HER and OER catalysis.

Furthermore, considering the excellent HER and OER performance of Pt@NiFeCo-E catalyst, we further explore the OWS performance by assembly the electrode Pt@NiFeCo-E//Pt@NiFeCo-E into a two-electrode alkaline electrolytic cell. To validate the bifunctionality of the Pt@NiFeCo-E catalyst, OWS performance were assessed by assembling the symmetric electrodes of Pt@NiFeCo-E//Pt@NiFeCo-E into a two-electrode alkaline electrolytic cell. As presented in Fig. 4a, the Pt@NiFeCo-E//Pt@NiFeCo-E electrodes exhibit excellent OWS activity, which only required an ultrasmall working potential of 1.42 V to achieve a current density of 10 mA cm^{-2} , superior to the Pt@NiFeCo//Pt@NiFeCo (1.52 V@10 mA cm^{-2}) and Pt/C//RuO₂ (1.54 V@10 mA cm^{-2}) electrodes, and lots of bubbles were generated on both electrodes. Furthermore, the Pt@NiFeCo-E//Pt@NiFeCo-E electrodes exhibited excellent stability with negligible potential decay at a current density of 100 mA cm^{-2} under a 50-h stability test (Fig. 4b). Besides freshwater, the Pt@NiFeCo-E catalyst also demonstrated excellent performance in seawater splitting reaction. Under the same test

conditions, as illustrated in Fig. 4c, the Pt@NiFeCo-E showed excellent OER activity in alkaline simulated seawater (fresh water + 0.5 M NaCl + 1.0 M KOH) (230 mV@100 mA cm^{-2}), which is better than that in 1.0 M KOH (234 mV@100 mA cm^{-2}). In real seawater with 1.0 M KOH, the catalyst only needed 277 mV to reach 100 mA cm^{-2} for OER. The excellent OER activity of Pt@NiFeCo-E enables excellent performance in overall seawater splitting (OSS). As shown in Fig. 4d, the symmetric Pt@NiFeCo-E electrodes only required potentials of 1719 and 1755 mV, respectively, to reach a current density of 100 mA cm^{-2} for alkaline simulating sea water (deionized water + 1.0 M KOH + 0.5 M NaCl) and real sea water (1.0 M KOH + seawater). Similar to deionized water splitting, the Pt@NiFeCo-E//Pt@NiFeCo-E electrodes exhibited robust durability with slight potential fluctuations at a current density of 100 mA cm^{-2} for 50 h. As shown in the insets in Fig. 4e, no morphology change occurred after 50 h the OSS reactions in both simulated sea water and real sea water.

We believed that the formation of 2Pt dimers and Pt pairs plays a vital role in the outstanding HER and OER activity and the bifunctionality of the Pt@NiFeCo-E catalyst. To reveal the catalytic origins and the structural effects of Pt dual atoms on the bifunctionality, DFT calculations were carried out [22]. NiFeCo LDH with Pt dimers (2Pt), Pt₂ and Pt nanoclusters (Pt_{NCS}) as the catalytic sites on the surface were constructed. The electron transfer behavior is quantitatively revealed by the calculated charge density differences (Fig. 5a–b) to explore the charge transfer between the Pt dual atoms (2Pt and Pt₂) and the substrates (NiFeCo LDH), where the yellow and cyan areas refer to the electron accumulation and electron depletion regions, respectively [45]. Electron accumulation (yellow) mainly occurs on O atoms with higher electronegativity, while Pt and Pt atoms have lower electronegativity and exhibit charge loss around the atom (cyan), and the accumulation and dissipation of charge indicate that a strong interaction between the Pt dual atoms and the substrate exists, which can regulate the electronic transfer of the catalyst and also provide strong anchoring to demobilize the dispersed atoms for durable stability [46]. The charge density differences of 2Pt-NiFeCo LDH and Pt₂-NiFeCo LDH interacting with adsorption/desorption H* or OOH* (Fig. S20–21) were calculated to explore the differences of adsorption/desorption behaviors of the 2Pt and the Pt₂ dual atoms. As shown in Fig. S20, a strong interaction between 2Pt and the substrate leads to the rearrangement of electrons and more positively charged 2Pt sites, which easily activate the reactants

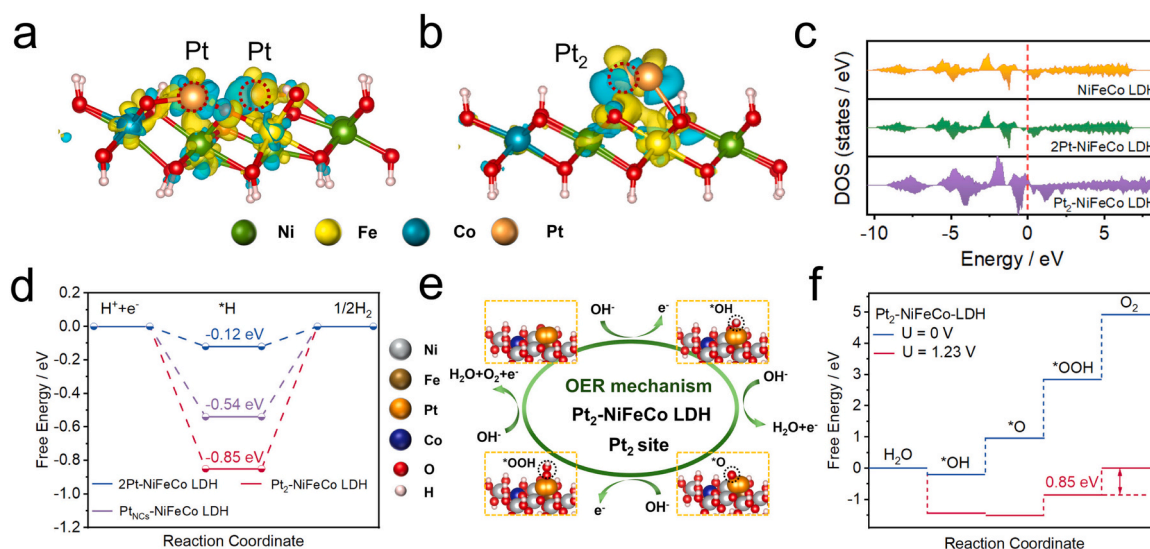


Fig. 5. Theoretical calculations on adsorption behaviors of 2Pt dimers and Pt₂ pairs loaded on NiFeCo LDH substrates. Differential charge density of (a) 2Pt-NiFeCo LDH and (b) Pt₂-NiFeCo LDH. (c) DOS of NiFeCo LDH, 2Pt-NiFeCo LDH, and Pt₂-NiFeCo LDH. (d) H* adsorption Gibbs free energy profile on 2Pt-NiFeCo LDH, Pt₂-NiFeCo LDH and Pt_{NCS}-NiFeCo LDH. (e) Optimized models and the corresponding OER catalytic mechanism. (f) Energy profile of OER steps occurring onto the Pt₂-NiFeCo LDH.

and enhance the adsorption of H^* intermediates, accelerating the HER reaction kinetics [47,48]. The interaction between the Pt_2 and the substrate is weaker (Fig. S21), which is conducive to the desorption of OOH^* . Bader charge analysis is used to calculate the charge redistribution at the 2Pt-NiFeCo LDH and Pt_2 -NiFeCo LDH interface. The addition of Pt causes electrons to accumulate at Pt and the aggregation of electrons at the adsorption site of the molecule facilitates the activation of reactants, resulting in optimized electrochemical kinetics [49]. Moreover, the bridge oxygen between Ni and Pt ions interacts with the hydrogen atom of the adsorbed H_2O molecule, attracting the electrons from the water molecule [50]. Both the bridge oxygen in 2Pt-NiFeCo LDH and Pt_2 -NiFeCo LDH show higher Bader charge and possess the higher ability to weaken the adsorption of H-O bonds in water (Fig. S22). All these results suggest that the loading of 2Pt and Pt_2 weakens the H-OH bond and promotes the dissociation of adsorbed H_2O molecules. The total DOS of NiFeCo LDH, 2Pt-NiFeCo LDH, and Pt_2 -NiFeCo LDH are shown in Fig. 5c, both of the Pt loaded catalysts are continuous at the Fermi level, indicating their conductive metallic properties.

Fig. S23 shows adsorption and dissociation free energies of water molecules on the 2Pt-NiFeCo LDH, Pt_2 -NiFeCo LDH and Pt_{NCs} -NiFeCo LDH. Pt_2 -NiFeCo LDH ($\Delta G_{H_2O} = 0.26$ eV) and Pt_{NCs} -NiFeCo LDH ($\Delta G_{H_2O} = 0.25$ eV) have comparable adsorption free energy of water molecules, illustrating the similar adsorption capability for water molecule. The free energy of water dissociation into H^* and OH^* is 0.26, 0.37 and 0.66 eV on 2Pt-NiFeCo LDH, Pt_2 -NiFeCo LDH and Pt_{NCs} -NiFeCo LDH, respectively. 2Pt-NiFeCo LDH has the best water dissociation capacity, the free energy change from water adsorption to dissociation on Pt_2 -NiFeCo LDH is 0.11 eV, which is much lower than that of 2Pt-NiFeCo LDH (0.55 eV) and Pt_{NCs} -NiFeCo LDH (0.41 eV), indicating that Pt_2 -NiFeCo LDH had a beneficial effect on accelerating the water adsorption and dissociation [51]. Gibbs free energy (ΔG_{H^*}) for hydrogen adsorption has been proven to be a reliable descriptor for the assessment of intrinsic HER activity, where a near-zero ΔG_{H^*} value can be balanced during hydrogen intermediate adsorption/desorption, maximizing the HER performance [52]. As shown in Fig. 5d, the ΔG_{H^*} of 2Pt-NiFeCo LDH (-0.12 eV) is close to the ideal value of 0 eV than that of the Pt_{NCs} -NiFeCo LDH (-0.54 eV) and Pt_2 -NiFeCo LDH (-0.85 eV), suggesting that 2Pt-NiFeCo LDH has good H^* adsorption kinetics during HER [53]. Further, the adsorption free energy of oxygen intermediates was calculated. As shown in Fig. 5e, the OER process consisting of three steps of OH^* , O^* , and OOH^* intermediates adsorptions/desorptions were examined. The optimal model is shown in Fig. 5e, S24–25. Based on the optimal model, the process of OOH^* translating into O_2 was the rate determining step (RDS) on Pt_2 -NiFeCo LDH, which has an energy barrier as low as only 0.85 eV (Fig. 5f). For the 2Pt-NiFeCo LDH and Pt_{NCs} -NiFeCo LDH configuration, the energy barrier from O^* to OOH^* is 1.73 eV and Pt_{NCs} -NiFeCo LDH is 1.44 eV, which suggesting that Pt_2 -NiFeCo LDH is more favorable to catalyze OER thermodynamically rather than HER. These theoretical calculations clearly show that the constructed the 2Pt dimers (2Pt-NiFeCo LDH) are favorable for HER catalysis while the Pt_2 pairs (Pt_2 -NiFeCo LDH) present the lowest energy barrier towards OER catalysis. Combining with the experimental results, we clarify that the bifunctionality of the Pt dual-atom catalysts originates from the formation of two types of Pt dual atomic structures which have distinct HER activity and OER activity respectively.

4. Conclusion

In summary, we constructed a well dispersed Pt dual atoms on cation vacancy-rich nickel-based hydroxides. Two distinct Pt dual atomic structures, 2Pt dimers with an interatomic distance of 2.6 Å and Pt_2 pairs with a distance of 0.9 Å, were successful formed onto the cationic vacancy-rich nickel-based hydroxide substrate. Contributed by the HER catalytic active 2Pt-NiCoFe-LDH and the OER favorable Pt_2 -NiCoFe-LDH, bifunctionality towards both HER and OER catalysis were achieved, which delivered excellent HER (14 mV@10 mA cm^{-2}) and OER

(234 mV@100 mA cm^{-2}) catalysis performance, and thus fascinating performance towards overall water splitting (1719 mV@100 mA cm^{-2} for fresh water and 1755 mV@100 mA cm^{-2} for real seawater) in the alkaline condition, which significantly outperforms the commercial Pt/C and most of the reported Pt-based catalysts. This work thus can provide inspirations in exploring more efficient precious metal-based electrocatalysts via proper atomic structure manipulation for bifunctional catalysis.

CRediT authorship contribution statement

Pengfei Zhang: Writing – original draft, Methodology, Investigation, Data curation. **Manyuan Gan:** Visualization, Data curation. **Yanhui Song:** Writing – review & editing, Supervision, Project administration, Funding acquisition. **Peizhi Liu:** Validation, Investigation. **Haojie Liang:** Validation, Data curation. **Yongqing Shen:** Validation, Investigation. **Bingshe Xu:** Validation, Formal analysis. **Ting Liao:** Validation, Formal analysis. **Junjie Guo:** Writing – original draft, Supervision, Resources, Funding acquisition. **Ziqi Sun:** Writing – review & editing, Validation, Supervision.

Declaration of Competing Interest

The authors declare that they have no known competing financial interests or personal relationships that could have appeared to influence the work reported in this paper

Data Availability

Data will be made available on request.

Acknowledgements

This work was supported by the National Natural Science Foundation of China (52201019, U21A20174, and 52001222), the Science and Technology Innovation Talent Team Project of Shanxi Province (202304051001010), the Key National Scientific and Technological Cooperation Projects of Shanxi Province (202104041101008), the Natural Science Foundation of Shanxi Province (202203021212244), the Program for the Innovative Talents of Higher Education Institutions of Shanxi (PTIT), and the Scientific and Technological Innovation Programs of Higher Education Institutions in Shanxi (STIP, 2022L036). T. L. and Z.S. acknowledged the Australian Research Council for its support through the Discovery Projects (DP200103568 and DP230101625) and the Future Fellowship projects (FT160100281 and FT180100387) and the Australian National Computational Infrastructure (NCI) Facility for the granted generous computational time. The authors acknowledge the assistance of Instrumental Analysis Center Taiyuan University of Technology. P. Zhang and M. Gan contributed equally to this work.

Appendix A. Supporting information

Supplementary data associated with this article can be found in the online version at doi:10.1016/j.apcatb.2024.124214.

References

- [1] Y. Tian, M. Wen, A. Huang, Q. Wu, Z. Wang, Q. Zhu, T. Zhou, Y. Fu, Significantly stabilizing hydrogen evolution reaction induced by Nb-doping Pt/Co(OH)₂ nanosheets, *Small* 19 (2023) 2207569, <https://doi.org/10.1002/sml.202207569>.
- [2] J. Xu, C. Zhang, H. Liu, J. Sun, R. Xie, Y. Qiu, F. Lü, Y. Liu, L. Zhuo, X. Liu, J. Luo, Amorphous MoO_x-stabilized single platinum atoms with ultrahigh mass activity for acidic hydrogen evolution, *Nano Energy* 70 (2020) 104529, <https://doi.org/10.1016/j.nanoen.2020.104529>.
- [3] Y. Song, B. Xu, T. Liao, J. Guo, Y. Wu, Z. Sun, Electronic structure tuning of 2D metal (hydr)oxides nanosheets for electrocatalysis, *Small* 17 (2021) 2002240, <https://doi.org/10.1002/sml.202002240>.

- [4] L. Ring, B.G. Pollet, M. Chatenet, S. Abbou, K. Kupper, M. Schmidt, M. Huck, A. Gries, M. Steinhart, H. Schafer, From bad electrochemical practices to an environmental and waste reducing approach for the generation of active hydrogen evolving electrodes, *Angew. Chem. Int. Ed.* 58 (2019) 17383–17392, <https://doi.org/10.1002/anie.201908649>.
- [5] F. Dionigi, Z. Zeng, I. Sinev, T. Merzdorf, S. Deshpande, M.B. Lopez, S. Kunze, I. Zegkinoglou, H. Sarodnik, D. Fan, A. Bergmann, J. Drnec, J.F. Araujo, M. Glicch, D. Teschner, J. Zhu, W.X. Li, J. Greeley, B.R. Cuenya, P. Strasser, In-situ structure and catalytic mechanism of NiFe and CoFe layered double hydroxides during oxygen evolution, *Nat. Commun.* 11 (2020) 2522, <https://doi.org/10.1038/s41467-020-16237-1>.
- [6] Y. Hu, G. Luo, L. Wang, X. Liu, Y. Qu, Y. Zhou, F. Zhou, Z. Li, Y. Li, T. Yao, C. Xiong, B. Yang, Z. Yu, Y. Wu, Single Ru atoms stabilized by hybrid amorphous/crystalline FeCoNi layered double hydroxide for ultraefficient oxygen evolution, *Adv. Energy Mater.* 11 (2021) 2002816, <https://doi.org/10.1002/aenm.202002816>.
- [7] C. Zhang, Y. Cui, Y. Yang, L. Lu, S. Yu, Z. Meng, Y. Wu, Y. Li, Y. Wang, H. Tian, W. Zheng, Highly conductive amorphous pentlandite anchored with ultrafine platinum nanoparticles for efficient pH-universal hydrogen evolution reaction, *Adv. Funct. Mater.* 31 (2021) 2105372, <https://doi.org/10.1002/adfm.202105372>.
- [8] W. Chen, Y. Ma, F. Li, L. Pan, W. Gao, Q. Xiang, W. Shang, C. Song, P. Tao, H. Zhu, X. Pan, T. Deng, J. Wu, Strong electronic interaction of amorphous Fe₂O₃ nanosheets with single-atom Pt toward enhanced carbon monoxide oxidation, *Adv. Funct. Mater.* 29 (2019) 1904278, <https://doi.org/10.1002/adfm.201904278>.
- [9] Z. Yang, S. Zhang, H. Zhao, A. Li, L. Luo, L. Guo, Subnano-FeO_x clusters anchored in an ultrathin amorphous Al₂O₃ nanosheet for styrene epoxidation, *ACS Catal.* 11 (2021) 11542–11550, <https://doi.org/10.1021/acscatal.1c01366>.
- [10] T. Pu, J. Ding, F. Zhang, K. Wang, N. Cao, E.J.M. Hensen, P. Xie, Dual atom catalysts for energy and environmental applications, *Angew. Chem. Int. Ed.* 62 (2023) e202305964, <https://doi.org/10.1002/anie.202305964>.
- [11] H. Yu, W. Wang, Q. Mao, K. Deng, Z. Wang, Y. Xu, X. Li, H. Wang, L. Wang, Pt single atom captured by oxygen vacancy-rich NiCo layered double hydroxides for coupling hydrogen evolution with selective oxidation of glycerol to formate, *Appl. Catal. B-Environ.* 330 (2023) 122617, <https://doi.org/10.1016/j.apcatb.2023.122617>.
- [12] P. Kuang, Y. Wang, B. Zhu, F. Xia, C.W. Tung, J. Wu, H.M. Chen, J. Yu, Pt single atoms supported on N-doped mesoporous hollow carbon spheres with enhanced electrocatalytic H₂-evolution activity, *Adv. Mater.* 33 (2021) 2008599, <https://doi.org/10.1002/adma.202008599>.
- [13] Y. Guo, M. Wang, Q. Zhu, D. Xiao, D. Ma, Ensemble effect for single-atom, small cluster and nanoparticle catalysts, *Nat. Catal.* 5 (2022) 766–776, <https://doi.org/10.1038/s41929-022-00839-7>.
- [14] H. Jeong, O. Kwon, B.-S. Kim, J. Bae, S. Shin, H.-E. Kim, J. Kim, H. Lee, Highly durable metal ensemble catalysts with full dispersion for automotive applications beyond single-atom catalysts, *Nat. Catal.* 3 (2020) 368–375, <https://doi.org/10.1038/s41929-020-0427-z>.
- [15] C. Chen, M. Sun, K. Wang, Y. Li, Dual-metal single-atomic catalyst: the challenge in synthesis, characterization, and mechanistic investigation for electrocatalysis, *SmartMat* 3 (2022) 533–564, <https://doi.org/10.1002/smm2.1085>.
- [16] X. Zheng, Y. Liu, Y. Yan, X. Li, Y. Yao, Modulation effect in adjacent dual metal single atom catalysts for electrochemical nitrogen reduction reaction, *Chin. Chem. Lett.* 33 (2022) 1455–1458, <https://doi.org/10.1016/j.cclet.2021.08.102>.
- [17] X. Hai, Y. Zheng, Q. Yu, N. Guo, S. Xi, X. Zhao, S. Mitchell, X. Luo, V. Tulus, M. Wang, X. Sheng, L. Ren, X. Long, J. Li, P. He, H. Lin, Y. Cui, X. Peng, J. Shi, J. Wu, C. Zhang, R. Zou, G. Guillen-Gosalbez, J. Perez-Ramirez, M.J. Koh, Y. Zhu, J. Li, J. Lu, Geminal-atom catalysis for cross-coupling, *Nature* 622 (2023) 754–760, <https://doi.org/10.1038/s41586-023-06529-z>.
- [18] Q. Miao, Z. Chen, X. Li, M. Liu, G. Liu, X. Yang, Z. Guo, C. Yu, Q. Xu, G. Zeng, Construction of catalytic Fe₂N₅P sites in covalent organic framework-derived carbon for catalyzing the oxygen reduction reaction, *ACS Catal.* 13 (2023) 11127–11135, <https://doi.org/10.1021/acscatal.3c02186>.
- [19] M. Jiao, Z. Chen, N. Wang, L. Liu, DFT calculation screened CoCu and CoFe dual-atom catalysts with remarkable hydrogen evolution reaction activity, *Appl. Catal. B-Environ.* 324 (2023) 122244, <https://doi.org/10.1016/j.apcatb.2022.122244>.
- [20] Y. Hu, Z. Li, B. Li, C. Yu, Recent progress of diatomic catalysts: general design fundamentals and diversified catalytic applications, *Small* 18 (2022) 2203589, <https://doi.org/10.1002/sml.202203589>.
- [21] W. Lai, P. Yu, L. Gao, Z. Yang, B. He, H. Huang, Boosting the interfacial hydrogen migration for efficient alkaline hydrogen evolution on Pt-based nanowires, *J. Mater. Chem. A* 10 (2022) 16834–16841, <https://doi.org/10.1039/d2ta05156g>.
- [22] L. Zhang, T. Yang, W. Zang, Z. Kou, Y. Ma, M. Waqar, X. Liu, L. Zheng, S. J. Pennycook, Z. Liu, X.J. Loh, L. Shen, J. Wang, Quasi-paired Pt atomic sites on Mo₂C promoting selective four-electron oxygen reduction, *Adv. Sci.* 8 (2021) 2101344, <https://doi.org/10.1002/adv.202101344>.
- [23] L. Wang, L. Zhang, W. Ma, H. Wan, X. Zhang, X. Zhang, S. Jiang, J.Y. Zheng, Z. Zhou, In situ anchoring massive isolated Pt atoms at cationic vacancies of α -Ni_{1-x}Fe_x(OH)₂ to regulate the electronic structure for overall water splitting, *Adv. Funct. Mater.* 32 (2022) 2203342, <https://doi.org/10.1002/adfm.202203342>.
- [24] P. Gao, Z. Chen, Y. Gong, R. Zhang, H. Liu, P. Tang, X. Chen, S. Passerini, J. Liu, The role of cation vacancies in electrode materials for enhanced electrochemical energy storage: Synthesis, advanced characterization, and fundamentals, *Adv. Energy Mater.* 10 (2020) 1903780, <https://doi.org/10.1002/aenm.201903780>.
- [25] O. Diaz-Morales, D. Ferrus-Suspedra, M.T.M. Koper, The importance of nickel oxyhydroxide deprotonation on its activity towards electrochemical water oxidation, *Chem. Sci.* 7 (2016) 2639–2645, <https://doi.org/10.1039/c5sc04486c>.
- [26] M.W. Louie, A.T. Bell, An investigation of thin-film Ni-Fe oxide catalysts for the electrochemical evolution of oxygen, *J. Am. Chem. Soc.* 135 (2013) 12329–12337, <https://doi.org/10.1021/ja405351s>.
- [27] J. Shan, C. Ye, S. Chen, T. Sun, Y. Jiao, L. Liu, C. Zhu, L. Song, Y. Han, M. Jaroniec, Y. Zhu, Y. Zheng, S.Z. Qiao, Short-range ordered iridium single atoms integrated into cobalt oxide spinel structure for highly efficient electrocatalytic water oxidation, *J. Am. Chem. Soc.* 143 (2021) 5201–5211, <https://doi.org/10.1021/jacs.1c01525>.
- [28] B.C. Cornilsen, X. Shan, P.L. Loyselle, Structural comparison of nickel electrodes and precursor phases, *J. Power Sources* 29 (1990) 453–466, [https://doi.org/10.1016/0378-7753\(90\)85018-8](https://doi.org/10.1016/0378-7753(90)85018-8).
- [29] M.C. Bernard, R. Cortes, M. Keddah, H. Takenouti, P. Bernard, S. Senyari, Structural defects and electrochemical reactivity of β -Ni(OH)₂, *J. Power Sources* 63 (1996) 247–254, [https://doi.org/10.1016/S0378-7753\(96\)02482-2](https://doi.org/10.1016/S0378-7753(96)02482-2).
- [30] H. Yu, S. Zhu, Y. Hao, Y.M. Chang, L. Li, J. Ma, H.Y. Chen, M. Shao, S. Peng, Modulating local interfacial bonding environment of heterostructures for energy-saving hydrogen production at high current densities, *Adv. Funct. Mater.* 33 (2023) 2212811, <https://doi.org/10.1002/adfm.202212811>.
- [31] W. He, R. Zhang, D. Cao, Y. Li, J. Zhang, Q. Hao, H. Liu, J. Zhao, H.L. Xin, Super-hydrophilic microporous Ni(OH)₂/Ni₃S₂ heterostructure electrocatalyst for large-current-density hydrogen evolution, *Small* 19 (2023) 2205719, <https://doi.org/10.1002/sml.202205719>.
- [32] L. Zhang, L. Han, H. Liu, X. Liu, J. Luo, Potential-cycling synthesis of single platinum atoms for efficient hydrogen evolution in neutral media, *Angew. Chem. Int. Ed.* 56 (2017) 13694–13698, <https://doi.org/10.1002/anie.201706921>.
- [33] Y. Liu, H.T.D. Bui, A.R. Jadhav, T. Yang, S. Saqlain, Y. Luo, J. Yu, A. Kumar, H. Wang, L. Wang, V.Q. Bui, M.G. Kim, Y.D. Kim, H. Lee, Revealing the synergy of cation and anion vacancies on improving overall water splitting kinetics, *Adv. Funct. Mater.* 31 (2021) 2010718, <https://doi.org/10.1002/adfm.202010718>.
- [34] Y. Hao, S.F. Hung, W.J. Zeng, Y. Wang, C. Zhang, C.H. Kuo, L. Wang, S. Zhao, Y. Zhang, H.Y. Chen, S. Peng, Switching the oxygen evolution mechanism on atomically dispersed Ru for enhanced acidic reaction kinetics, *J. Am. Chem. Soc.* 145 (2023) 23659–23669, <https://doi.org/10.1021/jacs.3c07777>.
- [35] Y. Chen, R. Ding, J. Li, J. Liu, Highly active atomically dispersed platinum-based electrocatalyst for hydrogen evolution reaction achieved by defect anchoring strategy, *Appl. Catal. B-Environ.* 301 (2022) 120830, <https://doi.org/10.1016/j.apcatb.2021.120830>.
- [36] J. Zhang, M. Wang, T. Wan, H. Shi, A. Lv, W. Xiao, S. Jiao, Novel (Pt-O_x)-(Co-O_x) nonbonding active structures on defective carbon from oxygen-rich coal tar pitch for efficient HER and ORR, *Adv. Mater.* 34 (2022) 2206960, <https://doi.org/10.1002/adma.202206960>.
- [37] L. Peng, N. Yang, Y. Yang, Q. Wang, X. Xie, D. Sun-Waterhouse, L. Shang, T. Zhang, G.I.N. Waterhouse, Atomic cation-vacancy engineering of NiFe-layered double hydroxides for improved activity and stability towards the oxygen evolution reaction, *Angew. Chem. Int. Ed.* 60 (2021) 24612–24619, <https://doi.org/10.1002/anie.202109938>.
- [38] H. Sun, L. Chen, Y. Lian, W. Yang, L. Lin, Y. Chen, J. Xu, D. Wang, X. Yang, M. H. Rummel, J. Guo, J. Zhong, Z. Deng, Y. Jiao, Y. Peng, S. Qiao, Topotactically transformed polygonal mesopores on ternary layered double hydroxides exposing under-coordinated metal centers for accelerated water dissociation, *Adv. Mater.* 32 (2020) 2006784, <https://doi.org/10.1002/adma.202006784>.
- [39] J. Lin, P. Wang, H. Wang, C. Li, X. Si, J. Qi, J. Cao, Z. Zhong, W. Fei, J. Peng, Defect-rich heterogeneous MoS₂/NiS₂ nanosheets electrocatalysts for efficient overall water splitting, *Adv. Sci.* 6 (2019) 1900246, <https://doi.org/10.1002/adv.201900246>.
- [40] T. Shinagawa, A.T. Garcia-Esparza, K. Takanabe, Insight on Tafel slopes from a microkinetic analysis of aqueous electrocatalysis for energy conversion, *Sci. Rep.* 5 (2015) 13801, <https://doi.org/10.1038/srep13801>.
- [41] J. Park, J. Theerthagiri, A. Min, C.J. Moon, M.Y. Choi, Laser-synthesized Ru-anchored few-layer black phosphorus for superior hydrogen evolution: role of acoustic levitation, *ACS Appl. Mater. Interfaces* 16 (2024) 11561–11574, <https://doi.org/10.1021/acsami.3c18427>.
- [42] Z. Wu, J. Mei, Q. Liu, S. Wang, W. Li, S. Xing, J. Bai, J. Yang, W. Luo, O. Guseynikova, A.P. O'Mullane, Y. Gu, Y. Yamauchi, T. Liao, Z. Sun, Phase engineering of dual active 2D Bi₂O₃-based nanocatalysts for alkaline hydrogen evolution reaction electrocatalysis, *J. Mater. Chem. A* 10 (2022) 808–817, <https://doi.org/10.1039/d1ta09019d>.
- [43] Z. Wu, T. Liao, S. Wang, W. Li, B. Wijerathne, W. Hu, A.P. O'Mullane, Y. Gu, Z. Sun, Volcano relationships and a new activity descriptor of 2D transition metal-Fe layered double hydroxides for efficient oxygen evolution reaction, *Mater. Horiz.* 10 (2023) 632–645, <https://doi.org/10.1039/d2mh01217k>.
- [44] Z. Zang, X. Wang, X. Li, Q. Zhao, L. Li, X. Yang, X. Yu, X. Zhang, Z. Lu, Co₉S₈ nanosheet coupled Cu₂S nanorod heterostructure as efficient catalyst for overall water splitting, *ACS Appl. Mater. Interfaces* 13 (2021) 9865–9874, <https://doi.org/10.1021/acsami.0c08202>.
- [45] S. Zhang, C. Tan, R. Yan, X. Zou, F.L. Hu, Y. Mi, C. Yan, S. Zhao, Constructing built-in electric field in heterogeneous nanowire arrays for efficient overall water electrolysis, *Angew. Chem. Int. Ed.* 62 (2023) e202302795, <https://doi.org/10.1002/anie.202302795>.
- [46] Y. Zhu, J. Sokolowski, X. Song, Y. He, Y. Mei, G. Wu, Engineering local coordination environments of atomically dispersed and heteroatom-coordinated single metal site electrocatalysts for clean energy-conversion, *Adv. Energy Mater.* 10 (2019) 1902844, <https://doi.org/10.1002/aenm.201902844>.
- [47] Z. Tao, H. Zhao, N. Lv, X. Luo, J. Yu, X. Tan, S. Mu, Crystalline/Amorphous-Ru/VO_x phase engineering expedites the alkaline hydrogen evolution kinetics, *Adv. Funct. Mater.* (2024) 2312987, <https://doi.org/10.1002/adfm.202312987>.

- [48] L. Guo, J. Chi, J. Zhu, T. Cui, J. Lai, L. Wang, Dual-doping NiMoO₄ with multi-channel structure enable urea-assisted energy-saving H₂ production at large current density in alkaline seawater, *Appl. Catal. B-Environ.* 320 (2023) 121977, <https://doi.org/10.1016/j.apcatb.2022.121977>.
- [49] Z. Zhao, Z. Li, Z. Zhang, X. Meng, Fe/P dual-doping NiMoO₄ with hollow structure for efficient hydrazine oxidation-assisted hydrogen generation in alkaline seawater, *Appl. Catal. B-Environ.* 347 (2024) 123805, <https://doi.org/10.1016/j.apcatb.2024.123805>.
- [50] M. Wang, J.Q. Wang, C. Xi, C.Q. Cheng, C.G. Kuai, X.L. Zheng, R. Zhang, Y.M. Xie, C.K. Dong, Y.J. Chen, X.W. Du, Valence-state effect of iridium dopant in NiFe(OH)₂ catalyst for hydrogen evolution reaction, *Small* 17 (2021) 2100203, <https://doi.org/10.1002/smll.202100203>.
- [51] Y. Feng, Z. Li, S. Li, M. Yang, R. Ma, J. Wang, One stone two birds: vanadium doping as dual roles in self-reduced Pt clusters and accelerated water splitting, *J. Energy Chem.* 66 (2022) 493–501, <https://doi.org/10.1016/j.jechem.2021.08.061>.
- [52] P. Zhai, M. Xia, Y. Wu, G. Zhang, J. Gao, B. Zhang, S. Cao, Y. Zhang, Z. Li, Z. Fan, C. Wang, X. Zhang, J.T. Miller, L. Sun, J. Hou, Engineering single-atomic ruthenium catalytic sites on defective nickel-iron layered double hydroxide for overall water splitting, *Nat. Commun.* 12 (2021) 4587, <https://doi.org/10.1038/s41467-021-24828-9>.
- [53] P. Zhou, G. Hai, G. Zhao, R. Li, X. Huang, Y. Lu, G. Wang, CeO₂ as an "electron pump" to boost the performance of Co₄N in electrocatalytic hydrogen evolution, oxygen evolution and biomass oxidation valorization, *Appl. Catal. B-Environ.* 325 (2023) 122364, <https://doi.org/10.1016/j.apcatb.2023.122364>.